

Recent Topics in Advanced Materials Science

Recent Topics in Advanced Materials Science:

Element by Element

By

Akio Makishima

Cambridge
Scholars
Publishing



Recent Topics in Advanced Materials Science: Element by Element

By Akio Makishima

This book first published 2019

Cambridge Scholars Publishing

Lady Stephenson Library, Newcastle upon Tyne, NE6 2PA, UK

British Library Cataloguing in Publication Data

A catalogue record for this book is available from the British Library

Copyright © 2019 by Akio Makishima

All rights for this book reserved. No part of this book may be reproduced, stored in a retrieval system, or transmitted, in any form or by any means, electronic, mechanical, photocopying, recording or otherwise, without the prior permission of the copyright owner.

ISBN (10): 1-5275-4029-4

ISBN (13): 978-1-5275-4029-3

TABLE OF CONTENTS

List of Figures.....	viii
List of Tables	xxv
Preface.....	xxvi
Part One: Topics for typical elements	
Section One	2
Physical constants and hydrogen related topics	
Section Two.....	17
Noble gas related topics	
Section Three.....	22
Lithium related topics	
Section Four	44
Topics for non-Be, B, Al, and Ga-In-Sn materials	
Section Five.....	60
Topics for alkali and alkali earth metals	
Section Six.....	75
Topics related to carbon	
Section Seven	96
Silicon and germanium related topics	
Section Eight	112
Pnictogen related topics	
Section Nine	149
Topics for oxygen, sulfur, selenium, and tellurium	

Section Ten	176
Halogen related topics	
Part Two: Transition element related topics	
Section Eleven	204
Transition metal related topics	
Section Twelve	245
Topics related for zirconium, hafnium, and tantalum	
Section Thirteen.....	252
Molybdenum and tungsten related topics	
Section Fourteen.....	263
Topics for ruthenium and osmium	
Section Fifteen.....	281
Rhodium and iridium related catalysts and complexes	
Section Sixteen	291
Palladium and platinum catalysts and complexes	
Section Seventeen.....	320
Topics for gold and mercury	
Part Three: Topics for lanthanide and actinide	
Section Eighteen.....	334
Topics for lanthanide and actinide	
Part Four: Interesting topics in materials science	
Section Nineteen.....	354
Catalysts for cars	
Section Twenty	361
Markovnikov's and anti-Markovnikov's reactions	

Section Twenty-one	370
Zeolite and luminescence related topics	
Section Twenty-two	377
Perovskite materials	
Section Twenty-three	384
MOF materials	
Section Twenty-four	393
Water harvesting and purifying systems	
Section Twenty-five	414
Functional polymers and sensors	
Section Twenty-six	436
Artistic molecules	
Section Twenty-seven	455
Molecular machines, machine learning and automation	
Section Twenty-eight	466
Ecological topics	

LIST OF FIGURES

- Fig. 1-1. Proton mass of each year. The horizontal axis is the published year. The vertical axis is $(M_x/M_{2017-1}) \times 10^{10}$. M_x means the mass published in year X.
Data: Borgenstrand (1997), Van Dyck et al. (1999), Bergström et al. (2002), Solders et al. (2008), and Heiße et al. (2017).
- Fig. 1-2. The shortest distance between hydrogens of two tri(3,5-*tert*-butylphenyl)methanes.
- Fig. 1-3. (a) The schematic diagrams of hydrogen spillover experiment. Support is from titanium oxide or aluminum oxide. A reduction of iron oxide only occurs when there is hydrogen spillover. (b) Aluminum oxide support. (c) Titanium oxide support.
- Fig. 1-4. Catalyst.
- Fig. 1-5. A kibble balance. The NIST-4 in the National Institute of Standards and Technology. Image credit: https://commons.wikimedia.org/wiki/File:NIST-4_Kibble_balance.jpg, Jennifer Lauren Lee, the U.S. National Institute of Standards and Technology (NIST).
<https://www.nist.gov/image/nist4wattbalance.jpg>.
- Fig. 1-6. (a) Catalysts for tritiation by T_2O . T_2O is available from T_2+PtO_2 in NMP (N-methyl-2-pyrrolidone). (b) $[^3H]$ Azithromycin, 28.0 Ci mmol⁻¹. The balls indicate the positions of the C-H bonds that are substituted by 3H with the % incorporation. (c) $[^3H]$ Fenspiride, 25.2 Ci mmol⁻¹.
- Fig. 1-7. Phases of water according to the temperature (the vertical axis).
- Fig. 2-1. The diamond anvil cell. (a) Two diamonds are facing with sandwiching a sample (box). The right side figure is a schematic diagram of a cross section of the sample, gasket, and diamond anvil. (b) The diamond anvil cell assembly. The arrow shows the place of the diamond anvils. (Photographs and figure credits: Dr. Shigehiko Tateno, Earth-Life Science Institute (ELSI), Tokyo Institute of Technology, Japan). This figure is published in "Biochemistry for Materials Sciences" by Akio Makishima Akio 2018. page 5, copyright: Elsevier.
- Fig. 2-2. The stable structure of Na_2He . This figure is published in "Biochemistry for Materials Sciences" by Akio Makishima 2018. page 5, copyright: Elsevier.
- Fig. 2-3. A surface diffraction isotope separator.
- Fig. 3-1. A Li plating test bath.
- Fig. 3-2. Monitoring Li ion by fluorescence.
- Fig. 3-3. α -Cyclodextrin, α -CD.
- Fig. 3-4. Nano-nets on silicon microparticle (SiMP) anodes. (a) Schematic and chemical compositions of nano-nets. (b) Pristine nano-nets on the SiMP anodes. (c) Stretched. (c) Recovered.
- Fig. 3-5. Calix[4]arene-strapped calix[4]pyrroles for the Li receptor.

Fig. 3-6. Crystal structure of the new cathode material for Li-ion batteries without Co. Image credit: Fujitsu Laboratories Ltd.

<http://www.fujitsu.com/global/about/resources/news/press-releases/2017/0529-01.html>

Fig. 3-7. Fabrication of flexible wire-shaped batteries.

Fig. 3-8. Solid oriented crystallites of Li_3OCl . The dotted lines show the interface, or grain boundary, between each crystallite. The solid line indicates the tilt angle between the grains.

Fig. 3-9. Rechargeable battery working at -70°C .

Fig. 3-10. Schematic of the bench scale column extraction setup. Brine, wash, and strip solutions are fed through the column, which is kept at 95°C . V1 and V2 are pinch valves. The valves and the pump are controlled by a computer.

Fig. 4-1. The crystal structure of $\text{Li}_2\text{B}_6\text{O}_9\text{F}_2$.

Fig. 4-2. Vitrimers. At high temperatures ($>T_v$), vitrimers can flow and behave like viscoelastic liquids.

Fig. 4-3. Schematic diagram of newly synthesized vitrimers.

Fig. 4-4. (a) A borenium cation. R is an σ -bound substitute. L is a ligand capable of occupying a third coordination site through π -backbonding. (b) The new borenium Lewis acid catalyst.

Fig. 4-5. (a) Contraction of six-membered cycle. (b) The total synthesis of artalbic acid (**4**). Et= ethyl, Bu= butyl.

Fig. 4-6. A schematic diagram of the gas bubbling system developed by Zavabeti et al. (2017).

Fig. 4-7. Nitrogen complexes by metal (the left column) and borylene (the right column).

Fig. 4-8. Synthesis of N_2 compounds.

Fig. 4-9. (a) Recyclable trifluoromethylation reagents. (b) Examples of trifluoromethylated compounds.

Fig. 4-10. *In vivo* borylation reaction between NHC-borane (A) and diazo ester (B) to yield organoboranes (C).

Fig. 5-1. The [2.2.2] cryptand.

Fig. 5-2. (a) Dendrimer and (b) dendron.

Fig. 5-3. Commonly encountered conformations of the $[\text{H}_2\text{NB}_2(\text{C}_6\text{F}_5)_6]^-$ anion. (a) When the anion is fully separated from the cation. (b) The anion undergoing M...F or CH...F contact with the cation. (c) Schematic presentation of the molecular structure of $\text{Cs}[\text{H}_2\text{NB}_2(\text{C}_6\text{F}_5)_6]$, showing the novel conformation C of the anion. (d) Tetracosahedral coordination geometry of 16-coordinate Cs^+ in **1**.

Fig. 5-4. Dimethylcalcium and its compounds. (a) Synthesis of dimethylcalcium $[\text{CaMe}_2]_n$ (**1**). (b) Synthesis of $[(\text{thf})_{10}\text{Ca}_7\text{Me}_{14}]$ (**2**). (c) Synthesis of $[(\text{thf})_3\text{Ca}(\text{Me})(\text{I})_2]$ (**3**). (d) Synthesis of $[(\text{thp})_5\text{Ca}_3(\text{Me})_5(\text{I})]$ (**4**). (e) Syntheses of $[(\text{Tp}^{\text{tBu,Me}})\text{Ca}(\text{Me})(\text{thf})]$ (**5a**) and $[(\text{Tp}^{\text{tBu,Me}})\text{Ca}(\text{Me})(\text{thp})]$ (**5b**). $\text{Tp}^{\text{tBu,Me}}$ = tris(3-^tBu-5-Me-pyrazolyl)borate. (f) Syntheses of $[(\text{thf})\text{Ca}(\text{O}(\text{tBu})_2\text{Me})_2]_2$ (**6**), $[(\text{tBu}_2\text{CO})\text{Ca}(\mu_2\text{-O}(\text{tBu})_2\text{Me})_3\text{-Ca}(\text{O}(\text{tBu})_2\text{Me})]$ (**7**) and $[\text{Ca}(\text{GaMe}_4)_2]_n$ (**8**).

Fig. 5-5. A. *Electrophorus electricus* has a main electric organ under its swimming muscles. B. Mechanism of voltage generation in electrocytes. Na^+ is pumped

- from the extra-cellular space to the electrocyte by the Na pump, and K^+ is pumped from the electrocyte to another extra-cellular space by the K pump. V_{oc} is open-circuit voltage. C. Mechanism of voltage generation in the artificial electric organ. When gels are out of contact, no voltage will be observed. However, mechanical contact brings a sequence of gels so that ionic gradients are connected across alternating charge-selective membranes, thereby producing potentials across each membrane that add up and can be stacked in a series of thousands of gels.
- Fig. 6-1. Molecular structure of $C_6(CH_3)_6^{2+}$. Counter anions and co-crystallized HSO_3F are omitted for clarity.
- Fig. 6-2. Triangulene.
- Fig. 6-3. (a) Polyadderene. (b) Unzipping reactions of polyadderene by mechanical force.
- Fig. 6-4. Textile-based triboelectric nanogenerators (TENGs).
- Fig. 6-5. Graphite-conjugated catalyst (GCC; a) and another catalyst, such as molecular and heterogenous catalysts (b and c, respectively).
- Fig. 6-6. Dissociation of a disaccharide. Each IR spectrum of a monosaccharide, which is dissociated at B, C, Y, and Z, fragments and is, therefore, different from the others.
- Fig. 6-7. (a) Annulative dimerization reaction. (b) Synthesis of graphene nanoribbon substructures.
- Fig. 6-8. Correlative imaging of Tasmanites. Correlative imaging and atomic force microscopy infrared spectroscopy (AFM-IR) characterization, where the Tasmanites outlined have one small mineral particle (indicated by the gray arrow), which has been transported inside. (a) Fluorescence microscopy, showing bright fluorescing Tasmanites. (b) Topographic image. (c) IR absorption mapping at 2920 cm^{-1} . (d) Mechanical stiffness mapping at 2920 cm^{-1} . Image credit: Yang et al. *Nature Communications*, 8, 2179.
- Fig. 7-1. Hydrocarbon C-H arylation reactions. R1= aryl, alkyl, halide, or silyl ether. WCA= weakly coordinating anion. TMS= trimethylsilyl.
- Fig. 7-2. The catalytic cycle.
- Fig. 7-3. Cross metathesis reaction between C-C and C-Si σ -bonds.
- Fig. 7-4. A monomeric SiO_2 complex.
- Fig. 7-5. Cagey silicophosphates. (a) **1**. $Ph_{12}Si_6P_4O_{16}$. (b) **2**. $Ph_{12}Si_6O_{16}P_4 \cdot 3B(C_6F_5)_3$. The tetrahedron shows the tetrahedron made by P atoms. The gray lines connect P and Si along each edge line of the tetrahedron for easier understanding of the structure. (c) and (d) Molecule cores of (c) **2P** and (d) **2M** representing opposite enantiomers when looked at vertically from P of $P=O$. Each crystal of (b) is built by one of these crystals. (e) **3**. $Ph_6Si_3O_8P_2 \cdot 2B(C_6F_5)_3$.
- Fig. 7-6. Schematic diagram showing electrochemical liquid phase epitaxy (ec-LPE).
- Fig. 7-7. Steps in the fabricating processes for surface invisible glasses. See text for explanation.
- Fig. 7-8. Schematic illustration of time-gated imaging of fingerprints with ZGO:Ga,Mn-COOH nanoparticles. (a) The nanoparticles are functionalized

- with carboxyl groups (ZGO:Ga,Mn-COOH). (b) The nanoparticles are treated with EDC/NHS (1-ethyl-3-(3-dimethylaminopropyl)-carbodiimide/N-hydroxysuccinimide) to form active ester on their surface. (c) The nanoparticles can react with intrinsic amino groups in the ridge of the fingerprint, forming strong labeling of the LFP. (d) Under excitation, the substrate shows strong background fluorescence and the fingerprint image can not be detected. (e) After excitation ceases, the background fluorescence decays rapidly, but the nanoparticles remain luminescent and, thus, the clear fingerprint image appears.
- Fig. 7-9. (a) Cytochrome c from wild-type *Rhodothermus marinus* (PDB 3CP5), which is modified from Stelter et al. (2008) and created using an NGL viewer (A.S. Rose et al. (2018) NGL viewer: web-based molecular graphics for large complexes). The bars and balls at the left side indicate heme. (b) The backbone style of the same protein. The amino acids of H49, M100, and M103 (His49, Met100, and Met103) are indicated by the boxes. The heme is indicated as dim balls.
- Fig. 7-10. Wild-type *R. marinus* cytochrome c becomes the enzyme (heme) that makes Me-EDA (**1**) into the organosilicon compounds (**3**) with high enantiomeric excess (ee) of >97 %.
- Fig. 8-1. (a) Triazolium ions. (b) Triazinium ion. (c) The nitrogen center atom of triazolium ion works as Lewis acids.
- Fig. 8-2. (a) The *cyclo-N₅⁻* ion. (b) 3,5-Dimethyl-4-hydroxyphenylpentazole (HPP). (c) m-Chloroperbenzoic acid (m-CPBA).
- Fig. 8-3. (a) Synthesis of MK-3682 (**3**) from chlorophosphoramidate (**1**) and nucleoside (**2**). Ph = phenyl. (b) Catalyst for the reaction (a). The stereoselectivity was 99:1.
- Fig. 8-4. Phosphorus heterocycles. (a) Syntheses of 1,3,4-azadiphospholides [1a], cyano-substituted [1b-1e] and siloxy compounds [1f-1i]. (b) Synthesis of 1-aza-2,3,4-triphospholenes.
- Fig. 8-5. Phospharubber. The results were $x \gg y, z$.
- Fig. 8-6. (a) Cyanuric acid. (b) Keto-form of cyanuric acid, which is more stable than (a). (c) The phosphorus analogue of cyanuric acid. (d)-(e)-(f)-(c). The synthesis route of (c). (g) A piano stool complex, $[\text{Mo}(\text{P}_3\text{C}_3(\text{OH})_3)(\text{CO})_3]$.
- Fig. 8-7. (a) Biradicaloid $[\text{P}(\mu\text{-N}(\text{Ter})_2\text{As})]$, Ter = 2,6-bis(2,4,6-trimethylphenyl)phenyl; (b) Mes* = 2,4,6-tri-*tert*-butylphenyl; (c) a new molecule containing four pnictogens, Mes*N(SbCl₂)AsPMes*.
- Fig. 8-8. (a) $[\text{ClAs}(\mu\text{-P-Ter})_2]$; (b) $[\text{ClSb}(\mu\text{-P-Ter})_2]$; (c) $[\text{ClBi}(\mu\text{-P-Ter})_2]$. Ter = 2,6-bis(2,4,6-trimethylphenyl)phenyl.
- Fig. 8-9. Bismuth (V) perfluoroalkylphosphinate.
- Fig. 8-10. The catalytic reactions of the bismuth(III) phosphinate $(\text{PhBi}[(\text{C}_2\text{F}_5)_2\text{PO}_2]_2)$. (a) Friedel-Crafts reaction. (b) and (c) Diels-Alder reactions.
- Fig. 8-11. A photograph of the Kawai-type high pressure apparatus (the multi-anvil high pressure apparatus) (5000 ton press) at the Institute for Planetary Materials (IPM). The arrow indicates the place of the guide-block, where cubic

- anvils are placed and pressed with the sample assembly. (Image credit: Dr. Daisuke Yamazaki, the Hacto group, IPM, Japan).
- Fig. 8-12. A conceptual image of the multi-anvils and the guide block. The guide block is based on the split spheres in the figure, in order to assemble the eight tungsten carbide (WC) cubic anvils. Only three split spheres of the guide block are drawn. In fact, the three faces pressing the cubic assembly are connected on each side of the guide-block, and one-axial press is used to press the cubic anvils.
- Fig. 8-13. (a) A photograph of the disassembled WC cubic anvils and the sample assembly is indicated by the arrow. The WC anvils are truncated to put the octahedral sample assembly. (Image credit: Dr. D. Yamazaki, the Hacto group, IPM.) (b) The sample assembly used for the synthesis of $\text{Cu}_{11}\text{Bi}_7$ by Clarke et al. (2016). (Image credit: Dr. D. Yamazaki, the Hacto group, IPM.)
- Fig. 8-14. Crystal structure of $\text{Cu}_{11}\text{Bi}_7$. The circles indicate Cu and Bi atoms, respectively. The upper and lower figures show views from c and b axes. Trigonal bipyramids formed by Cu atoms are shown as gray.
- Fig. 8-15. Crystal structure of FeBi_2 determined at 30 GPa by Walsh et al. (2016). The balls indicate Fe and Bi atoms, respectively.
- Fig. 8-16. A single nucleophilic attack from a Grignard reagent on a malonate-derived imine results in an unsymmetrical secondary product (top). A double attack from the same Grignard on the oxime produces a symmetrical secondary amine (bottom).
- Fig. 8-17. (a) IDPi catalyst. (b) [4+2]-cycloaddition of benzaldehyde (1) with 2,3-dimethyl-1,3-butadiene (2). Excellent yield and enantioselectivity (97%, 98:2 enantiometric ratio) were obtained.
- Fig. 8-18. BRD4592.
- Fig. 8-19. Triazenyl radicals.
- Fig. 8-20. A safe process for direct olefin diazidation.
- Fig. 8-21. New scheme for synthesizing phosphorus chemicals without using white phosphorus.
- Fig. 8-22. Cranberry harvest in New Jersey (Image credit: This image was released by the Agricultural Research Service, the research agency of the United States Department of Agriculture, with the ID K4418-6).
- Fig. 8-23. The cellulose repeating unit with phosphoethanolamine (shown in gray).
- Fig. 9-1. CuAAC reaction.
- Fig. 9-2. (a) Selectivity of SO_2F_2 and SOF_4 to aromatic hydroxyl and amino groups. (b) One example of multidimensional tetrahedral product.
- Fig. 9-3. Tetratriflylpropene, a new organic super acid.
- Fig. 9-4. (a) Mukaiyama adol reaction. (b) Hosomi-Sakurai acylation reaction. (c) Friedel-Crafts acylation reaction.
- Fig. 9-5. Schematic diagram of the new recycling system of NADP^+ .
- Fig. 9-6. Bis-thiourea catalyst.
- Fig. 9-7. An example of the carbohydrate connection.
- Fig. 9-8. Schematic diagram of quantum dots of CdSe with a band gap used in Caputo et al. (2017).

- Fig. 9-9. Reactions following the application of QDs. β -alkylation reaction is replaced from iridium catalysts by the QDs catalyst by Caputo et al. (2017).
- Fig. 9-10. 1-Ethyl-3-methylimidazolium bis(trifluoromethylsulfonyl)imide.
- Fig. 9-11. Synthesis of polysulfates.
- Fig. 9-12. (a) Togni's iodine (III) reagent. (b) Togni's tellurium analogs.
- Fig. 9-13. Oxyallyl precursors with furan derivatives generate bicyclic (4+3) cycloadducts. TMS= trifluoromethanesulfonate.
- Fig. 9-14. An easy synthesis method of acyl fluorides by $(\text{Me}_4\text{N})\text{SCF}_3$: Me= methyl; DCM= dichloromethane.
- Fig. 9-15. (a) A schematic diagram of a single Au-TBTP-Au junction for STM-BJ measurements. (b) Model of the electrochemically activated BTP switch. BTP shows the neutral and low-conductance state ("OFF"). On oxidation, BTP gains an antiaromatic character in the 6-4-6- π electron state that shows high conductance.
- Fig. 9-16. A new C_3 -symmetric tricyclic triol. (a) Chemical formula. (b) When seen through the C_3 axis.
- Fig. 9-17. Sulfone cross-couplings.
- Fig. 9-18. A cartoon showing the relation among the proto-Earth, the impactor, the giant impact, and the late veneer, in order of time. The gray areas indicate the metallic parts (core), which are denser than the silicates indicated in white.
- Fig. 10-1. Direct difluoromethylation from chlorodifluoromethane. (a) The reaction: Beg= ethyleneglycato boron: Bneop = neopentylglycolato boron. (b) Dibenzylideneacetone (dba). (c) Xantphos. (d) Hydroquinone. (e) 1,4-Dioxane.
- Fig. 10-2. Sequential C-CN bond borylation and difluoromethylation (a). See text for reaction conditions of (i), (ii), and (iii). (b) $[\text{RhCl}(\text{cod})]_2$ (Chloro(1,5-cyclooctadiene)rhodium(I)dimer). (c) 1,4-diazobicyclo[2,2,2] octane (DABCO).
- Fig. 10-3. Reaction converting phenol to aryl fluorides.
- Fig. 10-4 (a) The experiment setup of Tinoco et al. (2017). (b) Schematic diagram for the reaction. Ar= arene. DTE= 2-diazo-1,1,1-trifluoroethane. Image credit: NGL Viewer (A.S. Rose et al. (2018) NGL viewer: web-based molecular graphics for large complexes. Bioinformatics [doi:10.1093/bioinformatics/bty419](https://doi.org/10.1093/bioinformatics/bty419)), and PDB 1MBN. This figure is published in "Biochemistry for Materials Sciences" by Akio Makishima, 2018, page 249, copyright: Elsevier.
- Fig. 10-5. Flow scheme of continuous total synthesis of ciprofloxacin hydrochloride. This figure is published in "Biochemistry for Materials Sciences" by Akio Makishima 2018, page 250, copyright: Elsevier.
- Fig. 10-6. Synthesis of chiral homopropagyl β -amino alcohol.
- Fig. 10-7. Conventional C-H iodination methods.
- Fig. 10-8. The iodination of hydrocarbons using 1-iodo-3,5,5-trimethylhydantoin.
- Fig. 10-9. DDT (1,1,1-trichloro-2,2-bis(4-chlorophenyl)-ethane).
- Fig. 10-10. Classification of elements based on behavior in dilute HF.
- Fig. 10-11. Fluorinated diketide.
- Fig. 10-12. Comparison of the molecule and isolated atom at a high fluence of X-rays. The darkness of the color shows the electrons that remain in the atom. (a)

- The case of the isolated atom. In this case, two step X-rays arrive in sequence. At the first irradiation, iodine, carbon, and hydrogens are ionized (a-2). Following the second irradiation, only the iodine atom is ionized (a-3) and no further ionization from (a-2) occurs for carbon and hydrogens. The total charge state is 47+. (b) The case of the CH₃I molecule. Following the first irradiation, the case is the same (b-2). However, electrons are supplied from the methyl group to the iodine, thereby forming C⁴⁺ and 3H⁺ (b-3). Following the second irradiation, the iodine atom is ionized again. The total charge state is 54+.
- Fig. 11-1. The oxidation states of titanium and oxygen in TiO₂.
- Fig. 11-2. A Cr(CN^{4Bu}Ar₃NC)₃ complex synthesized by Büldt et al. (2017).
- Fig. 11-3. (a) A new method converting alkenes to 1,2-diazides. (b) The proposed catalytic cycle. V: power supply.
- Fig. 11-4. Decarboxylative alkenylation. (a) Basic reaction. (b) Prostaglandin synthesis. R=Ac.
- Fig. 11-5. Metallocenes. (a) Metallocene. (b) Ferrocene.
- Fig. 11-6. Polynickelocene switching between stable and dynamic states.
- Fig. 11-7. (a) (bpy-1)Ni(COD) (bpy-1= 2,2'-bipyridyl, COD= 1,5-cyclooctadiene). (b) Zn(HMDS)₂ (HMDS= hexamethyldisilazane). (c) Ir[dF(CF₃)-ppy]₂(dtbbpy)PF₆ (dF(CF₃)ppy= 2-(2,4-difluorophenyl)-5-(trifluoromethyl)pyridine, dtbbpy= 4,4'-di-*tert*-butyl-2,2'-bipyridine) (d) BnOH (benzyl alcohol).
- Fig. 11-8. New polymerization method of OCAs (O-carboxyanhydrides).
- Fig. 11-9. The atomic arrangements of the würtzite structures. (a) Atomic arrangement of a crystal structure of tetrahedral würtzite structures of ZnO. (b) Structure of ZnO with different planes.
- Fig. 11-10. (a) A chelating coordination units with a central 2,2'-bipyridine and two terminal triazolyl-pyridine. (b) A three metal helicate, L₃CuFeZn(OTf)₆. L= (a), OTf= CF₃SO₃⁻.
- Fig. 11-11. Preparation graphitic shell-encapsulated Co nanoparticles supported on carbon using MOF precursors (Jagadeesh et al., 2017).
- Fig. 11-12. Examples of the Co-DABCO-TPA@800-catalyzed reactions. (a) Reductive amination of aldehydes. (b) Reductive amination of ketones. (c) Syntheses of secondary and tertiary amines.
- Fig. 11-13. Iron-catechol complex.
- Fig. 11-14. Schematic diagram of a small subsection of the polyamidoxime fiber.
- Fig. 11-15. DFT-optimized geometries of V⁵⁺ complexes. **a** V⁵⁺ complexes with glutarimide-dioxime (H₃IDO). **b** DFT-optimized geometries of V⁵⁺ complexes with acetamidoxime (HAO). Image credit: A.S. Ivanov, Leggett, C.J., Parker, B.F., Zhang, Z., Arnold, J., et al. 2017. Origin of the unusually strong and selective binding of vanadium by polyamidoximes in seawater. *Nature Communications* 8, 1560. DOI: 10.1038/s41467-017-01443-1.
- Fig. 11-16. (a) Enantioselective synthesis of the antidepressant (2R,6R)-hydroxynorketamine. (b) A new Mn catalyst. (c) A transition state for the enantioselective conversion of the starting material of (a) with the Mn catalyst.
- Fig. 11-17. Schematic illustration of Ti₃C₂T_x films and their atomic structure (T= O, OH or F).

- Fig. 11-18. Synthesis of bio-derived surfactant. The yield is 54 %.
- Fig. 11-19. Chemical structures of L₁, L₂, and L₃
- Fig. 11-20. Photolysis of organic thiols with ferrous irons.
- Fig. 11-21. Hertzsprung-Russell diagram (H-R diagram). The Hertzsprung-Russell diagram. The horizontal axis is the color index, B-V, or the spectral type from O to M (at the top). The vertical axis is the logarithms of luminosity against the sun. AGB means the asymptotic giant branch stars.
- Fig. 11-22. Type Ia supernova. Type Ia supernova is considered to be the fate of the twin stars. In the twin star system, one star is the red giant, and one star is the white dwarf, of which mass density is far higher than the red giant. Therefore, a great deal of mass is transferred from the red giant onto the white dwarf. On the white dwarf, the mass becomes heavier than the Chandrasekhar limit, resulting in the explosive elemental formation. This causes a supernova, which is known as a type Ia supernova. There are type Ib or type Ic supernovae depending on the spectra of the supernovae.
- Fig. 11-23. Schematic diagram of instruments on the Hitomi (ASTRO-H) spacecraft. Image credit: JAXA.
http://global.jaxa.jp/projects/sat/astro_h/instruments.html.
- Fig. 11-24. Schematic diagram of the rocket microgravity laboratory. Configuration and optical paths of the double wavelength Mach-Zehnder-type laser interferometer with a nucleation chamber (vp) is shown. The lines show the optical paths of the red and green lasers, respectively. The resulting images of interference fringes are recorded with a charge-coupled camera (cam). The evaporation source (es) of Fe wire wrapped around a tungsten (W) filament 0.3 mm in diameter and 68 mm in length is placed in the chamber (n). “b”, “d”, “e”, “g”, “m”, “t”, “v”, “gl”, “py”, “rl”, “va”, and “vp” indicate beam splitter, dichroic mirror, electrode, gas line, mirror, thermocouple, vacuum gauge, green laser, pyrometer, red laser, valve, and view port, respectively.
- Fig. 11-25. Syn-F4 catalyzes the ferric enterobactin to dimer, monomer (not shown), and trimer, as the ferric enterobactin esterase occurs.
- Fig. 12-1. Synthesis of the tetrablock copolymer. 1: The isoselective pyridylamidohafnium catalyst. ⁱPr: isopropyl. 2, 4: Propylene. 3, 5: Ethylene. 6: Tetrablock copolymer.
- Fig. 12-2. The images of the pincer ligands. M is a metal, and A and B are a central donor (A in b) and a link to a lateral donor (B in c), respectively.
- Fig. 12-3. [CCC]X₃-donor pincer ligands for tantalum. (a) [κ^3 -Ar^{Tol2}]-Ta(PMe₃)₂Me₂. (b) [κ^3 -Ar^{Tol2}]-Ta(PMe₃)₂(η^6 -C₆H₆).
- Fig. 13-1. The Mo (or W) catalyst.
- Fig. 13-2. Synthesis of cis, syndiotactic A-alt-B copolymers by a Mo (or W) catalyst, [M]
- Fig. 13-3. Converting benzene ring to cyclohexenes by the complex TpW(NO)(PMe₃)(η^2 -PhCF₃) (a). This figure is published in “Biochemistry for Materials Sciences” by Akio Makishima 2018, page 251, copyright: Elsevier.
- Fig. 13-4. One-pot synthesis using the Ag₄₈Pd₅₂/WO_{2.72} catalyst. (a) One-pot aromatization of 2-nitrophenol and aldehyde to benzoxazole. (b) One-pot

- hydrogenation of ArR-NO₂ to ArR-NH₂. (c) One-pot aromatization of 2-nitroacetophenone and aldehyde to quinazolines.
- Fig. 13-5. a-Molybdenum diboride (a-MoB₂).
- Fig. 13-6. Ultrathin layers of transition-metal dichalcogenides (2D-TMD) device for photodetection. The input light is enhanced by the e-h pair generation effect by 350 %. The thickness of each element is at the single-atomic level. The small voltage is supplied by electrodes.
- Fig. 13-7. Cross-sectional view of "Atomristors".
- Fig. 13-8. (a) The $\epsilon^{94}\text{Mo}$ vs. $\epsilon^{95}\text{Mo}$ plot. (b) The $\epsilon^{183}\text{W}$ vs. $\epsilon^{182}\text{W}$ plot. NC and CC indicate the "non-carbonaceous" iron meteorite group and the "carbonaceous chondrite" iron meteorite group, respectively.
- Fig. 14-1. A schematic diagram of a molecular assembly for overall water splitting reaction. PS, WOC, and HEC indicate a photosensitizer, a water oxidation catalyst, and a hydrogen evolving catalyst. (The figure is modified from Kärkäs et al., 2014)
- Fig. 14-2. A schematic diagram of photosystem II, in which a Mn₄CaO₅-cluster oxidizes water into O₂+4H⁺+4e⁻.
- Fig. 14-3. The typical ruthenium (II) polypyridyl-type complex, [Ru(bpy)₃]²⁺ where bpy means 2,2'-bipyridine.
- Fig. 14-4. The blue dimer.
- Fig. 14-5. The Ru WOC, *in, in*-[[Ru(tpy)(H₂O)]₂(μ -bpp)]³⁺.
- Fig. 14-6. [Ru(bda)bpb]₃. bda = 2,2'-bipyridine-6,6'-dicarboxylic acid; bpb = 1,4-bis(pyrid-3-yl) benzene.
- Fig. 14-7. Lewis acid catalyzed enantioselective cycloaddition of 2'-hydroxychalcone. (OTf: trifluoromethanesulfonate or CF₃SO₃; t-BuPyBox: see Fig. 14-8; *i*-Pr: isopropyl; OAc: acetate; CFL: compact fluorescent lamp; rt: room temperature).
- Fig. 14-8. The chiral stereodifferentiating ligand, t-BuPyBox. t-Bu is tert-butyl.
- Fig. 14-9. The p _{π} -d _{π} -p _{π} π -conjugation.
- Fig. 14-10. The anti-aromatic five membered rings of osmium.
- Fig. 14-11. CCCC-pentadentate chelates of osmium.
- Fig. 14-12. (a) A new ruthenium catalyst. (b) The selectivity of the catalyst.
- Fig. 14-13. (a) An experimental set up. Ru catalysts are attached to a glass slide via a polymer chain and a magnetic particle, and pulled up by a pair of magnetic tweezers. (b) The reaction follows the Wait and Jump steps.
- Fig. 14-14. (a) The Ru catalyst **1** and the norbornene probe **2**, which only flashes when ring-opening metathesis polymerization (ROMP) occurs in the stationary condition. Mes= 2,4,6-trimethylphenyl. Cy= cyclohexane (-C₆H₁₁). (b) A spatiotemporal resolution experiment which reveals reaction dynamics through molecular catalysts within polymers. Option A: Catalysis occurs in the solution, which means no areas glow. Option B: Catalysis occurs after precipitation, thus glowing lights are observed.
- Fig. 14-15. (a) Fundamental carbon species. (b) Carbynes and equivalents. (c), (d), and (e) Arene C-H diazomethylation.
- Fig. 15-1. Rh catalyst for C-C and C-H bonds activations. (a) Total reaction. (b) Details of the reaction (the reactions are simplified). (A) The shaded circles

- indicate the positions. **(B)** Rh cuts the five member ring. **(C)** C-C activation, and Rh forms the six member ring. **(D)** C-H activation, and Rh forms another six member ring. **(E)** Rh is removed with forming a new six member ring and a methyl.
- Fig. 15-2. New Rh catalyst.
- Fig. 15-3. Synthesis of 1-phenylalkenes via oxidative arene vinylation.
- Fig. 15-4. (a) Schematic diagram of site-specific modification of an antibody by dirhodium metalloprotein catalyst (1) using alkyne-functionalized diazo (2). 1. Structure of dirhodium complex attached to carboxylate group of glutamic acid residue on the peptide. (b) The dirhodium core acts as a reactive catalytic center through metalcarbene formation and a coordination site for Lewis basic side chain in a protein. (c) Schematic diagram of azide-alkyne cycloaddition reaction (click chemistry) between alkyne-functionalized antibodies and azide-fluorophore (shown as a ball). Fluorophore can be added to cancer drugs.
- Fig. 15-5. (a) 1,3-Dialkylimidazolium, (b) 1,3-butadiene. (c) $\text{Ir}(\text{CO})_2$ on $\gamma\text{-Al}_2\text{O}_3$ in ionic liquid coating.
- Fig. 15-6. (a) Dirhodium catalysts for the non-activated secondary and tertiary C-H bonds. (b) An example of the reaction of the tertiary C-H bonds to the dirhodium catalyst.
- Fig. 16-1. Chiroptical sensing by Pd(II) complex. Ph = phenyl, R = various groups. TBAOH is tetrabutylammonium hydroxide, $(\text{C}_4\text{H}_9)_4\text{NOH}$.
- Fig. 16-2. Tested amino acids by De los Santos and Wolf (2016).
- Fig. 16-3. Examples of important molecules with β -lactams. (a) Penicillin (antibiotic); (b) Zetia (cardiovascular drug); (c) Chartelline C (natural product).
- Fig. 16-4. Synthesis of β -lactams.
- Fig. 16-5. Enantioselective intermolecular coupling phenols and allylic alcohols.
- Fig. 16-6. The intermolecular oxa-Heck reaction by the Pd catalyst.
- Fig. 16-7. Heck reactions. (a) The Heck reaction. (b) Mizoroki et al. (1971). (c) Heck et al. (1972).
- Fig. 16-8. Dimetalated pincer complexes. (a) SCS pincer of Loeb and Shimizu; (b) van Koten's NCN pincer; (c) NCN pincer used by Shinoya in a molecular "ball bearing"; (d) Dipalladium (II) complex of Lohrman et al. (2016).
- Fig. 16-9. Pt complex with Lewis acidic Sb-ligand. (a) $(o\text{-(Ph}_2\text{P)C}_6\text{H}_4)_2\text{SbCl}_2\text{-PtCl}$ (1). (b) $((o\text{-(Ph}_2\text{P)C}_6\text{H}_4)_2\text{SbOTf}_2)\text{PtCl}$ (2). When a nucleophilic substrate such as an alkyne reacts with (b), platinum reactive site is unmasked (see arrows) leaving (c) without a chloride removing reagent.
- Fig. 16-10. Reactions catalyzed by the Pt complex, 2 (Fig. 16-9b).
- Fig. 16-11. Schematic diagram of the catalytic bifunctional template.
- Fig. 16-12. A template material, a yield, and site selectivity. Ac-Gly-OH and HFIP are N-acetyl-protected glycine ligand and hexafluoroisopropanol. (a) A reaction targeting phenylpyridine. (b) A reaction targeting quinolone.
- Fig. 16-13. (a) Preparation of $(\text{CH}_3)_2\text{CHCONHAr}_F$ from isobutyryl chloride. Isobutyryl chloride is easily formed from the reaction of isobutyric acid with SOCl_2 . (b) Enantioselective C-H arylation of isobutyric acid. (c) Enantioselective C-H alkenylation and alkynylation of isobutyric acid.

- Ar(Het)= (hetero)aryl group; Ar_F=4-(CF₃)C₆F₄; Me= Methyl; TFA= trifluoroacetate; TIPS= triisopropylsilyl group.
- Fig. 16-14. (a) C-S metathesis reaction by palladium catalyst. (b) Depolymerization of thermoplastic polymer. (c) Late-stage derivatization (i.e. direct modification of the final product) of an antipsychotic drug.
- Fig. 16-15. Platinum-containing cancer drugs. (a) Cisplatin. (b) Oxaliplatin. (c) Carboplatin. This figure was published in “Biochemistry for Materials Sciences” by Akio Makishima 2018, page 181, copyright: Elsevier.
- Fig. 16-16. (a) Starting materials. (b) The product identified in 1964. (c) The corrected composition of the product in 2017. (Ph = phenyl).
- Fig. 16-17. (a) Secondary electron microscope (SEM) image of the PdAu nanoparticle. (b) Up. Two dimensional histogram of product positions on the nanoparticle in (a) in $50 \times 50 \text{ nm}^2$ bins. The nanoparticle has been reoriented to align horizontally. Outer white line, white circle, and the contour of the Au particle are determined from the SEM image in (a). (b) Down. Segmentation of a typical PdAu nanoparticle: regions of monometallic Pd (Pd), Au-doped Pd next to the Pd–Au interface (PdAu), monometallic Au (Au), and Pd-doped Au next to the Pd–Au interface (AuPd). Image credit: Chen, G., Zou, N., Chen, B., Sambur, J. B., Choudhary, E., et al. 2017. Bimetallic Effect of Single Nanocatalysts Visualized by Super-Resolution Catalysis Imaging. *ACS Central Science*, 3, 1189–1197. (c) Proposed chemical equation of photodriven disproportionation reaction of resazurin (Rz[•]) to resorufin (Rf) and a one-electron-oxidized radical species (Rz^{•+}) catalyzed by Pd or Au catalysts.
- Fig. 16-18. Conversion of Pd and Au into water-soluble complexes by mild conditions. (a) Traditional methods. (b) New methods.
- Fig. 16-19. (a) The tested Suzuki-Miyaura cross-coupling reaction. (b) Heat output (kJ) according to time by Yang et al. (2018). (c) Chemical formulas of Pd(dppf)Cl₂, DMSO, DMF, and dioxane.
- Fig. 16-20 Pd catalyst for C-H fluorination.
- Fig. 17-1. The schematic diagram of the stable crystal with α -cyclodextrin [AuBr₄]⁻ and K⁺.
- Fig. 17-2. Schematic diagram for direct gold-nanoparticle integration by laser ablation.
- Fig. 17-3. All-metal aromatic sandwich Au-Sb cluster [Sb₃Au₃Sb₃]³⁻.
- Fig. 17-4. New synthesis of the rheumatoid arthritis drug leflunomide (Arava), which shows a new trifluoromethylation reaction.
- Fig. 17-5. Phosphine-calixarene gold chloride complexes used as precursors for the synthesis of Au clusters (a) a1, a2, and (b).
- Fig. 17-6. Nanoparticle surfactants make a monolayer skin on a droplet: X= Fe₃O₄ or PbS.
- Fig. 18-1. The structure of [La(η^4 -Sb₄)₃]³⁻. La can be replaced with Y, Ho, Er, or Lu.
- Fig. 18-2. Formation of Chromogen I to GlcNAc.
- Fig. 18-3. (a) The arrangement of nine Ln³⁺ ions of [Ln₉(μ_4 -O)(μ_3 -OH)₈(LH)₄(OAc)₄(H₂O)₁₂] 5ClO₄·24H₂O (Ln = Gd or Dy). (b) The coordination of LH²⁻, where L is Chromogen I.

- Fig. 18-4. Single-molecule magnet (SMM); $[\text{Dy}(\text{Cp}^{\text{III}})_2][\text{B}(\text{C}_6\text{F}_5)_4]$ with $\text{Cp}^{\text{III}} = \{\text{C}_5\text{H}_2^{\text{tBu}}\text{Bu}_{3-1,2,4}\}$ and $^{\text{t}}\text{Bu} = \text{C}(\text{CH}_3)_3$.
- Fig. 18-5. Molecular structure of Ce *bis*(carbene) complex ($[\text{M}(\text{BIPM}^{\text{TMS}})_2]$; $\text{M} = \text{Ce}, \text{U}, \text{Th}$; $\text{BIPM}^{\text{TMS}} = \{\text{C}(\text{Ph}_2\text{PNSiMe}_3)_2\}^{2-}$) at 150K. The structures of U and Th complexes are very similar. Hydrogen atoms and lattice solvent are not shown for clarity.
- Fig. 18-6. Crystal structure of a berkelium coordination compound. The central Bk(III) ion is coordinated by three monoprotonated dipicolinate ligands in tridentate O,N,O fashion.
- Fig. 18-7. Thorium and uranium complexes.
- Fig. 18-8. (a) 6-Carboxyfluorescein–glucose. (b) Dysprosium–1,4,7,10-tetraazacyclododecane–1,4,7,10-tetraacetic acid–glucose (Glc-DOTA-Dy(III)).
- Fig. 18-9. Mechanism of the Pt-CeO₂ catalyst. A. An oxygen vacancy exists in the catalyst. B. The oxygen vacancy moves to the surface of the catalyst. C. When a water molecule comes, it is absorbed in the vacancy, and Pt-Ce-OH groups are formed. These sites become active sites for CO oxidation.
- Fig. 18-10. Cerium containing methanol dehydrogenase from *Methylacidiphilum fumariolicum* SolV by Pol et al. (2014). Image Credit: NGL Viewer (A.S. Rose et al. (2018) NGL viewer: web-based molecular graphics for large complexes. Bioinformatics doi:10.1093/bioinformatics/bty419), and RCSB PDB 4MAE.
- Fig. 19-1. Potassium tert-butoxide/ hydrosilane (KOSi) homogeneous hydrodesulfurization.
- Fig. 19-2. (a) Ru catalyst, Ru-11. (b) Pd catalyst, IC-1. (c) Ru catalyst, Ru-CAAC. (d) The target reaction (isomerization ethenolysis of RME).
- Fig. 20-1. Markovnikov's rule. (a) Hydration. (b) Oxidation. The reactant in the parentheses shows one against Markovnikov's rule.
- Fig. 20-2. The anti-Markovnikov hydrations of alkenes. (a) Indirect synthesis of alcohols from olefins with anti-Markovnikov selectivity. (b) Grubbs' triple relay catalysis system. Shvo's catalyst = see (c); BQ = benzoquinone; Bu = butyl; Ph = phenyl; Pr = propyl. (c) The Shvo's catalyst (Shvo and Czarkie, 1986). Ph = phenyl. (d) The new anti-Markovnikov hydration of alkenes via the radical cation by Hu et al. (2017). (e) The ACR⁺-Mes⁻ catalyst. Ph = phenyl.
- Fig. 20-3. Proposed mechanism of a new anti-Markovnikov hydration by Hu et al. (2017).
- Fig. 20-4. (a) The anti-Markovnikov law reaction with a new enzyme, aMOx. (b) The structure of P450 monooxygenase PikC (PDB: 2WHW) without the heme from Li et al. (2009) is shown. This is the base structure of aMOx. Image credit: NGL Viewer (A.S. Rose et al. (2018) NGL viewer: web-based molecular graphics for large complexes. Bioinformatics doi:10.1093/bioinformatics/bty419), and PDB 2WHW.
- Fig. 21-1. Cu-zeolites catalyst. In the model by Paolucci et al. (2017), Cu ions with NH₃ travels to form oxygen-bridged dimer complexes. (Figure is based on Jacoby (2017).)

- Fig. 21-2. (a) An electron-donating molecule, N,N,N',N'-tetramethylbenzidine (TMB). (b) An electron-accepting molecule, 2,8-bis(diphenylphosphoryl)dibenzo[b,d]thiophene (PPT).
- Fig. 22-1. Crystal structures of (a) α - (DMEN)PbBr₄ (DMEN = 2-(dimethylamino)ethylamine); (b) (DMAPA)PbBr₄ (DMAPA = 3-(dimethylamino)-1-propylamine); (c) (DMABA)PbBr₄ (DMABA = 4-dimethylaminobutylamine).
- Fig. 22-2. 1931 color space chromaticity diagram. Image credit: Wikipedia. https://upload.wikimedia.org/wikipedia/commons/3/3b/CIE1931xy_blank.svg.
- Fig. 22-3. (a) Optical images under ambient light and 365 nm UV lamp. (b) Steady-state PL emission spectra of MAPbX₃ NCs@Pb-MOF. (1: MAPbCl₃, 2: MAPbCl₂Br, 3: MAPbClBr₂, 4: MAPbBr₃, 5: MAPbBr₂I, 6: MAPbBrI₂, 7: MAPbI₃). Image Credit: Zhang, C., Wang, B., Li, W., Huang, S., Kong, L. et al. 2017. Conversion of invisible metal-organic frameworks to luminescent perovskite nanocrystals for confidential information encryption and decryption. *Nature Communications*, 8: 1138. DOI: 10.1038/s41467-017-01248-2.
- Fig. 23-1. Cuboctahedron building unit. (a) Cuboctahedron is made of six square faces and eight triangle faces. One center and three corners of one triangle face are composed of the uranium node (UO₂(RCOO)₃) and three organic linkers, respectively. (b) Two cuboctahedron cages are connected by a single triangular face.
- Fig. 23-2. (a), (c), (e), and (g). From secondary pentagonal to tertiary icosidodecahedron structures. (b), (d), (f), and (h). From secondary hexagonal to tertiary rectified hexakaidecahedron structures.
- Fig. 23-3. (a) and (c). The quaternary tetrahedron structure is formed from the tertiary icosidodecahedron structure (the left ball indicates the structure of Fig. 23-2g). The connecting bond corresponds to the pentagon prism in Figs. 23-2a, c, and e. (b) The quaternary tetrahedron structure is formed from the tertiary rectified hexakaidecahedron structure (the right ball indicates the structure of Fig. 23-2h). The connecting bond that corresponds to the hexagon prism appears in Figs. 23-2b, d, and f. (d) The quaternary diamond-topology structure is formed from the tetrahedron structure of (b). (e) The final structure of NU-1301 is formed by putting the tetrahedron of (b) into the space of the diamond structure (d).
- Fig. 23-4. Schematic diagram of monolithic and powder MOF synthesis. (a) A metal and organic ligand solution were mixed. (b) HKUST-1 primary particles were made. (c) Wet gel is formed. (d) Powder was made at a high temperature or under a vacuum. (e) Dense monolithic MOF, _{mono}HKUST-1 was made under mild drying conditions.
- Fig. 23-5. (a) Structure of BODCA-MOF. (b) ¹H NMR spectra of crystalline BODCA-*d*-MOF.
- Fig. 24-1. Schematic diagram of a water harvesting system.
- Fig. 24-2. (a) H₂BTDD (bis(1H-1,2,3-triazolo [4',5'-i])dibenxo[1,4]dioxin). (b) Structure of Co₂Cl₂(BTDD) (I) projected along the *c* axis. Hydrogen atoms are omitted for clarity. At low relative humidity (RH), water is absorbed at the

- open coordination sites of the Co atoms, decreasing the pore diameter from above to below. Image credit: Rieth et al. (2017), American Chemical Society.
- Fig. 24-3. Comparison of MOF and zeolites investigated for water sorption. Materials that take up water between 10% and 30% RH are desirable for their strong affinity for water and their relative ease of regeneration. The rightmost "1" shows the work of Rieth et al. (2017). RH indicates the relative humidity. Image credit: Rieth et al. (2017), American Chemical Society.
- Fig. 24-4. Water purification column using polyoxometalate supported liquid phases (POM-SILPs) based on lipophilic POM-ILs supported on porous silica.
- Fig. 24-5. Aquaporin-1. 1J4N by Sui et al. (2001) from PDB. (a) The top view. The protein is embedded through the membrane in this direction. The water molecule passes the membrane through the channel in the center. (b) The side view. The pass of water is covered with hydrophobic α -helix structures. Image credit: NGL Viewer (A.S. Rose et al. (2018) NGL viewer: web-based molecular graphics for large complexes. Bioinformatics doi:10.1093/bioinformatics/bty419), and PDB 1J4N.
- Fig. 24-6. (a) Perfluorooctanoic acid (PFOA) and (b) β -cyclodextrin (β -CD).
- Fig. 24-7. DFB-CDP (decafluorobiphenyl-cyclodextrin) polymers.
- Fig. 24-8. Possible modes of binding **1** (Meisenheimer complex) with different metal ions and the fluoride anion.
- Fig. 24-9. (a) Tree and seed pods of *Moringa oleifera*. Image credit: https://commons.wikimedia.org/wiki/User:Harveychl#media/File:The_tree_and_seedpods_of_Moringa_oleifera.JPG. (b) *Moringa* seeds. Image credit: https://commons.wikimedia.org/wiki/File:The_seeds_of_Moringa_oleifera.JPG. The photographs A and B were taken by Prof. Chen Hualin.
- Fig. 24-10. *Moringa* seed extract-functionalized sand (*f*-sand) filter. Cationic and antimicrobial proteins in *Moringa* seeds can be dissolved easily and adsorbed onto a sand surface, changing the charge of the sand particles to positive. As pathogens and dirt have a negative charge, this filter removes them.
- Fig. 25-1. The reaction between meta-xylylenediamine (MXDA) and CO₂, which form anhydrous white precipitates (MXDA·CO₂).
- Fig. 25-2. The Grignard reaction.
- Fig. 25-3. (a) Highly stretchable polymer semiconductor film. (b) Chemical compositions of the semiconducting polymer DPPT-TT and the soft-elastmer (SEBS).
- Fig. 25-4. Gas permeable polymers. (a) PTMSP. (b) PIM-1. (c) PIM-TMN-Trip.
- Fig. 25-5. (a) Schematic representation of the selected tripeptide sequences. Each "D F Y" indicates one of the amino acid shown in (b). (b) When X is D, F, or Y in NH₂-CHX-COOH, the amino acid becomes aspartic acid, phenylalanine, or tyrosine, respectively. There are six types of sequences, DFY, DYF, YFD, FYD, FDY, and YDF. Tyrosine is oxidized to phenol, DOPA, and dopaquinone (arrows from left to right) by tyrosinase.
- Fig. 25-6. Self-healing gels. (a) The figure shows the enlarged shape of the gels from the frustrated Lewis pairs (FLPs). Gray lines indicate borane (B) and phosphine (P) functionalized polystyrenes. The short black line connecting B and P shows a diethyl azodicarboxylate molecule, which promotes rapid

- network formation. (b) The chemical formula in the box is the enlarged Lewis acid (P) and base (B) interaction.
- Fig. 25-7. Two polymerizable azo-derivatives: (I) a hydrogen-bonded azopyridine, and (II) a hydroxyl group in the ortho position. Each azo-derivative (7 mol%) was copolymerized with a mixture of a liquid-crystal monoacrylate (RM23, 42 mol%) and a liquid-crystal diacrylate (RM82, 50 mol%), initiated by 1 mol% of the photoinitiator, Irgacure 819 (not shown).
- Fig. 25-8. Mechanism of wave propagation. Schematic diagram of the experimental set-up, showing a polymeric film, under an incidence light source. The small black objects in the film show the azobenzene molecules, which isomerize to cis under the light, resulting in shrinking of the film and causing the force (the small arrows). The shaded parts of the ribbon isomerize back to trans and expand causing the force shown by the round arrows.
- Fig. 25-9. Whisky sensor. (a) The three most discriminating sensor array elements (PAE tongues). (b) GFP fluorescent protein tongues (GFPs tongues). GFP-K36 and GFP-E36 are positively and negatively charged, respectively.
- Fig. 25-10. (a) 1-(-)-Menthol. (b) Nutmeg neolignan (stereomixture). (c) An 8-O-4'-neolignan derivative.
- Fig. 25-11. (a) Dipeptide probe. (b) D-Lactate analog.
- Fig. 25-12. Photosensitive hydrogel.
- Fig. 25-13. Schematic representation of the single molecule detection device structure.
- Fig. 25-14. Schematic illustration of “freeze-spinning” technique, combining “directional freezing” with “solution spinning”. This realizes the continuous and large-scale fabrication of biomimetic fibers with aligned porous structures, mimicking polar bear hair. The silk fibroin solution extruded from a pump controlled syringe is gradually frozen when it passes through a cold copper ring. The frozen fiber is freeze-dried to keep its porous structure. Finally it is woven into a textile. The fiber diameter is $\sim 200 \mu\text{m}$.
- Fig. 26-1. Knot topology. The grey color indicates the basic building block of each knot. The number in (a)–(c) shows the Alexander-Briggs notation. The main number indicates the number of crossings, and the subscript differentiates the knot from others with the same number of crossings (see text). (a) 3_1 (trefoil). (b) 5_1 (pentafoil). (c) 8_{19} . (d) Solomon link. (e) Linear double helicates. (f) Star of David.
- Fig. 26-2. The synthesis method of the molecular with 8_{19} knot.
- Fig. 26-3. Evolution of “sulflower” molecules. (a) Persulfurated benzene (C_6S_6). (b) Fully-substituted circulene (C_{16}S_8). (c) Persulfurated coronene ($\text{C}_{24}\text{S}_{12}$).
- Fig. 26-4. Various carbon nanotubes (CNTs) and carbon nanobelts. (a) Carbon nanotubes (CNTs). (b) Carbon nanobelts. (c) Carbon nanobelt (fused arene system). (d) Carbon nanoring (linked arene system).
- Fig. 26-5. Synthesis route of the Itami belt.
- Fig. 26-6. The synthesis of the pentanuclear complex, $[\text{Pd}_5(\mathbf{L1})_5(\mathbf{L2})_5](\text{BF}_4)_{10}$, where $\mathbf{1}$ is the molecular star. $\text{DMSO} = (\text{CH}_3)_2\text{SO}$.
- Fig. 26-5. A double helical SnIP. (a) Crystal structure projected from a-axis. The $[\text{SnI}]$ and $[\text{P}]$ helices form a double helical SnIP strand. The box shows the unit

- shell. The M and P helices are left- and right-handed. (b) Schematic diagram of the double helix arrangement. The [SnI] and [P] helices rotate along the hypothetical axis, which is shown as the white rod. The captions are the same with (a).
- Fig. 26-7. (a) DNA-based components from the top to the center; the top, triangular brick with three identical recessed docking sites; the next white, V-shaped brick with a different protruding plug pattern on each outward-pointing face; grey, V-shaped white brick; the center, connector brick with docking sites on each of the wide face. (b) The component of (a) was self-assembled to form 1.2 GDa dodecahedron with a diameter of 450 nm.
- Fig. 27-1. (a) Molecular structures of a rotaxane-based molecular machine. Final forms as amino acids are phenylalanine, leucine, and alanine for $n = 1, 2, \text{ and } 3$, respectively. (b) Schematic diagram of rotaxane's ring and thread, and the sequential synthesis of amino acids. As the first ring goes out, the next amino acid (gray balls) is added.
- Fig. 27-2. Schematic diagram of iterative coupling of building blocks indicated by different colors.
- Fig. 27-3. (a) A molecular structure of a molecular machine with the arm at the left side. (b) The same machine with the arm at the right side. Only the joint part is shown. (c) An example of a product (S)-(S). (d) A schematic figure of the molecular machine. When the arm of is at the left side. (e) A schematic figure of the molecular machine. When the arm is at the right side. Only the arm after the joint is shown.
- Fig. 27-4. A ligand pool used in the machine learning by Janet et al. (2018).
- Fig. 27-5. The palladium-catalyzed Buchwald-Hartwig cross-coupling reaction.
- Fig. 27-6. Experimental design and analysis (a) Multidimensional discovery of catalytic coupling reactions. (b) An alkyne hydroallylation and a nickel-catalyzed variant of alkyne diarylation.
- Fig. 27-7. A molecular platform and a rotatable positioning arm. A. The top view. B. The side view.
- Fig. 28-1. (a) Syringaresinol. (b) Bisphenol A.
- Fig. 28-2. Function and requirements for sunscreens (photoprotector).
- Fig. 28-3. Structures of (a) mycosporine-glycine and (b) palythine. (c) Core structures of possible sunscreens.
- Fig. 28-4. A safer and greener route to methyl nitroacetate.
- Fig. 28-5. Tropylium catalyst.
- Fig. 28-6. Triclosan.
- Fig. 28-7. Schematic illustration of transforming bulk natural wood to super-strong and tough densified wood. Step 1: Chemical treatment to partially removal of lignin/hemicellulose; Step 2: Mechanical hot pressing at 100 °C, which reduces to a thickness of 80 %. Most densified wood consists of well aligned cellulose nanofibres, which enhance hydrogen bond formation among neighbouring nanofibers.
- Fig. 28-8. A. Hydrosilylation of CO_2 by R_3SiH to afford sequentially bis(silyl)acetal, $\text{H}_2\text{C}(\text{OSiR}_3)_2$, and CH_4 ($\text{R}_3\text{SiH} = \text{PhSiH}_3, \text{Et}_3\text{SiH}, \text{ and } \text{Ph}_3\text{SiH}$). B. [1], $[\kappa^3\text{-Tism}^{\text{PriBenz}}]\text{MgH}$. [2], $\{[\text{Tism}^{\text{PriBenz}}]\text{Mg}\}[\text{HB}(\text{C}_6\text{F}_5)_3]$.

Fig. 28-9. Green route to indigo. A. Indican. B. Indoxyl. C. Indigo.

Fig. 28-10. SEM and EDX images of a uranium-bearing particle in soil from the Dressing Floor location (25 cm) (the horizontal scale is almost 10 cm). Image credit: Corkhill et al. (2017), *npj Mat. Degrad.*, 1, Article number: 19.

LIST OF TABLES

Index of periodic tables

A. Parts One, Two, and Three (Sections One to Eighteen).

B. Part Four (Sections Nineteen to Twenty-eight).

The superscript and subscript numbers after the element symbol indicate the section numbers, where the elements are treated as a priority and as subordinate, respectively.

Table 10-1. The twenty amino acids; each amino acid has a three-letter and a one-letter abbreviation.

Table 17-1. Appropriate sizes of cyclodextrin with gold anions and alkali cations

Table 19-1. Relative prices of precious metals. Values are normalized to Pt=1. The price of platinum is \$940 /Oz, €28.4 /g, ¥3480 /g or £24.8 /g. The prices of 1 g powder from the Nilaco corporation catalog (2016) are used.

Table 24-1. Pollutant removal properties of the POM-SILPs.

PREFACE

In this book, topics of organic chemistry are not separated from those of inorganic chemistry. This has not been done before. Most organic chemistry topics appear from section twelve (Zr, Hf, and Ta) to section sixteen (Pd and Pt), because these elements form new complexes and work as catalysts for reactions in organic chemistry.

Part Four discusses specific topics not included in Parts One, Two, and Three. These topics include catalysts for cars (section nineteen), anti-Markovnikov reactions (twenty), zeolites and luminescence (twenty-one), Perovskites materials (twenty-two), MOF materials (twenty-three), water harvesting and purification (twenty-four), functional polymers (twenty-five), artistic molecules (twenty-six), molecular machines (twenty-seven), and ecological topics (twenty-eight).

You will notice that this book discusses materials science in terms of industrial, inorganic, and organic chemistry, but contains only a few mentions of biochemistry or life-related-sciences, which form a large proportion of this field today. Of course, this can be inferred from the title, and the author intentionally removed such topics because these topics have been summarized in another of the author's books, *Biochemistry in Materials Science: Catalysts, Complexes and Proteins* (Makishima, 2018). The books, therefore, act as a companion to each other.

Index of periodic tables.

A. Part One, Two and Three (Sections from One to Eighteen)

H ^{1,2}	ELEMENT ^{Main} _{Sub} Section number																		He ²
Li ^{3,4,6,10}	Be ⁴																	F ^{9,10}	Ne ²
Na ^{5,8}	Mg ^{8,10}																	O ^{8,9,10,14,16,18}	F ^{9,10,14,16,18}
K ^{5,6,10,15,18}	Ca ^{5,10,14}	Sc ¹⁴	Ti ^{14,11}	V ¹¹	Cr ^{6,11}	Mn ^{7,14}	Fe ^{8,11}	Co ^{8,10,11}	Ni ^{8,9,11}	Cu ^{8,9,11,15,16}	Zn ^{7,10,12,14,17}	Ga ^{7,8,9}	Ge ⁸	As ⁸	Se ^{8,13}	Br ^{16,17}	Kr		
Rb ⁵	Sr	Y ¹⁸	Zr ^{8,12}	Nb ¹⁰	Mo ^{9,11,13}	Tc	Ru ^{9,14}	Rh ^{10,15}	Pd ^{8,10,13,16}	Ag ^{13,16,17}	Cd ^{9,11}	In ⁶	Sn ^{5,8}	Sb ^{8,16,18}	Te ^{9,10}	I ^{9,10,16}	Xe ¹⁰		
Cs ⁵	Ba	L	Hf ¹²	Ta ^{10,12}	W ^{4,8,13}	Re	Os ¹⁴	Ir ^{9,11,15}	Pt ^{16,17,18}	Au ^{9,16,17}	Hg ¹⁷	Tl ⁶	Pb ^{12,8,9,17}	Bi ⁸	Po	At	Rn		
Fr	Ra	A	Rf	Db	Sg	Bh	Hs	Mt	Ds	Rg	Cn	Nh	Fl	Mc	Lv	Ts	Og		

B. Part Four (Sections from Nineteen to Twenty-eight)

H ^{24,26}	ELEMENT ^{Main} _{Sub} Section number																												He	
Li	Be																											Ne		
Na ^{24,28}	Mg ^{25,28}																											N ^{19,25,27,28}	O ^{19,21,24,25,27,28}	F ^{24,25,26,28}
K ²⁸	Ca	Sc	Ti	V	Cr ¹⁴	Mn	Fe ²⁶	Co ²⁴	Ni ^{24,27}	Cu ^{17,23,26,24}	Zn ²³	Ga	Ge	As ²⁶	Se	Br ^{20,22,26,27}	Kr													
Rb	Sr ²¹	Y	Zr ^{19,24}	Nb	Mo	Tc	Ru ^{19,20,26}	Rh ¹⁹	Pd ^{19,20,26,27}	Ag ^{21,23}	Cd ²⁴	In	Sn ²⁶	Sb	Te	I ^{22,26}	Xe													
Cs	Ba	L	Hf	Ta	W ²⁴	Re	Os	Ir	Pt ^{19,20}	Au ²¹	Hg ²⁴	Tl	Pb ^{22,24}	Bi	Po	At	Rn													
Fr	Ra	A	Rf	Db	Sg	Bh	Hs	Mt	Ds	Rg	Cn	Nh	Fl	Mc	Lv	Ts	Og													
L	La	Ce ¹⁸	Pr ¹⁸	Nd ¹⁸	Pm	Sm	Eu ¹⁸	Gd ¹⁸	Tb ¹⁸	Dy ¹⁸	Er ¹⁸	Tm	Yb	No	Lr															
A	Ac	Th ¹⁸	Pa ⁵	U ^{5,11,18}	Np ¹⁸	Pu ¹⁸	Am	Cm ¹⁸	Bk ¹⁸	Cf	Es	Fm	Md	No	Lr															
																												He		
																												Ne		
																												Ar		
																												Kr		
																												Xe		
																												Rn		
																												Og		
L	La	Ce ¹⁹	Pr ¹⁹	Nd	Pm	Sm	Eu	Gd	Tb	Dy	Er	Tm	Yb	No	Lr															
A	Ac	Th	Pa	U ^{23,28}	Np	Pu	Am	Cm	Bk	Cf	Fm	Md	No	Lr																

The author was once a pure materials-scientist in a company. Then he became an analytical geochemist in the Institute for Study of the Earth's Interior (ISEI), Okayama University at Misasa, which has been recently renovated into the Institute for Planetary Materials (IPM). He achieved his professorship in 2006 in ISEI, and he has published over 60 scientific papers. He had to give up research activities at 55 years old because of his health problems, and so he became an author of modern sciences. He has already published three books: *Thermal Ionization Mass Spectrometry (TIMS): Silicate Digestion, Separation and Measurement* (Makishima 2016); *Origins of the Earth, Moon, and Life: An Interdisciplinary Approach* (Makishima 2017); and *Biochemistry in Materials Science: Catalysts, Complexes and Proteins* (Makishima 2018). This is his fourth book. These books represent his wide interests in science. The author is very much fascinated by the beauty of inorganic materials, as well as biochemical materials, especially the chemical formulae of inorganic complexes as described in section twenty-six of this book.

References

- Makishima, Akio. 2016. *Thermal ionization mass spectrometry (TIMS). Silicate digestion, Separation, Measurement*. Weinheim: Wiley-VCH Verlag GmbH & Co. KGaA.
- Makishima, Akio. 2017. *Origins of the Earth, Moon and Life: a Multidisciplinary Approach*. Amsterdam: Elsevier.
- Makishima, Akio. 2018. *Biochemistry in Materials Science: Catalysts, complexes and proteins*. Amsterdam: Elsevier.

PART ONE:
TOPICS FOR TYPICAL ELEMENTS

SECTION ONE

PHYSICAL CONSTANTS AND HYDROGEN RELATED TOPICS

Chapter 1.1. The new proton's atomic mass

Heiße et al. (2017) reported the precise measurement of a single proton's atomic mass with a purpose-built Penning-trap system. A comparison with the previous data is shown in Fig. 1-1.

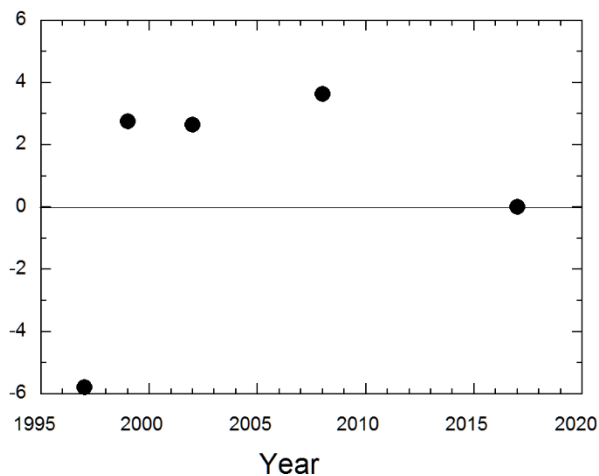


Fig. 1-1.